3D Variations in Viscosity Reconcile the Strength of the Lower Mantle Inferred from Glacial Isostatic Adjustment and Mantle Convection

A. Bellas-Manley[1], K. Kang[2], T.W. Becker[2,3,4] & R.S. Nerem[1,5]

[1]Colorado Center for Astrodynamics Research, Department of Aerospace Engineering Sciences, University of Colorado Boulder

[2]Institute for Geophysics, Jackson School of Geosciences, The University of Texas at Austin

[3]Department of Earth and Planetary Sciences, Jackson School of Geosciences, The University of Texas at Austin

[4]Oden Institute for Computational Engineering & Sciences, The University of Texas at Austin

[5]Cooperative Institute for Research in Environmental Sciences, University of Colorado Boulder

Key points

- Considering 3D-viscosity in models of GIA reconciles a persistent discrepancy in mantle viscosity inferred from GIA and mantle convection
- Models of GIA with 3D-viscosity can accommodate an upper/lower mantle viscosity contrast consistent with mantle convection models ($\Delta\eta$~30)
- A GIA model with 3D-viscosity and $\Delta\eta$~30 significantly improves the fit to a range of observational constraints compared to previous models

In press at Geophys. Res. Lett., April 2026

Abstract

A widely accepted global model of glacial isostatic adjustment (GIA) is based on ICE-6G ice loading and 1D-viscosity model VM5a, a viscosity profile which remains at odds with mantle convection constraints such as from geoid modeling. We explore 3D-viscosity variations in models of GIA and show that a model with lateral viscosity variations (LVVs) scaled from seismic tomography and lower mantle viscosity compatible with mantle convection constraints (~30 times upper mantle viscosity) significantly reduces the misfit to relative sea level (~40%), $\dot{J}_2$ (60%), and polar motion (75%) while incurring only a small misfit penalty (~5%) for GNSS-uplift compared to VM5a, which has lower mantle viscosity ~6 times upper mantle viscosity. Regional results exhibit additional tradeoffs but indicate that comparable solutions might be found with additional model refinement. The origin of a longstanding disagreement on lower mantle viscosity may thus be resolved by accounting for LVVs in models of GIA.

Plain Language Summary

Glacial isostatic adjustment (GIA) is the solid Earth response to the melting of ice sheets since the end of the last ice age, and models of this process are primarily constrained by observations of relative sea level (RSL) and uplift rates from satellite geodesy (GNSS). To fit these observations, GIA studies often assume that the viscosity of the mantle varies with depth only and find that the lower mantle is less than ten times stronger than the upper mantle. This modest increase is inconsistent with mantle convection constraints which imply that the lower mantle must be stronger (30-100 times more viscous than the upper mantle) to fit observations including the geoid and slab sinking rates. We show that this disagreement can be reconciled if models of GIA are formulated with 3D-viscosity where lateral variations are scaled from seismic tomography. Our preferred new model has a strong lower mantle (30 times upper mantle viscosity), significant lateral viscosity variations, and improves the fit to RSL records (40%), changes in the Earth's oblateness (60%), polar motion rates (75%), and incurs only a small penalty in the misfit to measured crustal uplift rates from GNSS (5%).

Introduction

Glacial isostatic adjustment (GIA) is an important global process that interacts with ice sheet dynamics (*Weertman*, 1964; *Gomez et al*., 2024; *Houriez et al.*, 2025), glacial cycles (*Han et al*., 2021; *Berends et al*., 2021), lithospheric plate motions (*Yuan & Zhong*, 2025), and provides important constraints on absolute mantle viscosity (*Haskell,* 1935; *Cathles*, 1975; *Mitrovica,* 1996). A commonly accepted model of GIA is based on the ice loading history ICE-6G and the 1D-radial mantle viscosity profile VM5a (*Argus et al.*, 2014; *Peltier et al*., 2015). The ICE-6G/VM5a GIA model is widely used to correct data including satellite altimeter measurements of sea surface height (*Beckley et al*., 2017), uplift from GNSS (*Lau et al.*, 2020), time-variable gravity from GRACE and GRACE-FO (*Landerer et al.*, 2020), and changes in Earth oblateness from satellite laser ranging (*Nerem & Wahr*, 2011). GIA models thus have a significant impact on studies of hydrology, ice mass loss, sea level, and global change.

The viscosity of the lower mantle matters for such models. Early GIA calculations were interpreted to preclude a highly viscous lower mantle based on crustal uplift rates which require lower mantle viscosity ~10^{21}-10^{22} Pa s, equivalent to a viscosity contrast $\Delta\eta < 10$ times that of the upper mantle (*Cathles*, 1975; *Peltier & Andrews*, 1976). However, the observed static geoid can be reproduced by mantle convection models with density inferred from seismic tomography only if $\Delta\eta$=30-100 (*Hager*, 1984; *Hager & Richards*, 1989), an inference confirmed by subsequent inversions (e.g., *King*, 1995; *Panasyuk & Hager*, 2000). Models of mantle convection likewise indicate a preference for slab slowdown and accumulated slab material below reconstructed convergent margins consistent with a similar increase in lower mantle viscosity (e.g., *Ricard et al.,* 1993; *Lithgow-Bertelloni & Richards,* 1998; *Steinberger et al.*, 2010). Such strong lower mantle viscosity also reproduces a range of other dynamical constraints including supercontinent-cycles, and true polar wander (e.g., *Bunge et al.*, 1996; *Steinberger & O'Connell*, 2002; *Rolf et al.*, 2018; *Li & Zhong*, 2009; *Mao & Zhong*, 2021).

That $\Delta\eta$ inferred from GIA is significantly lower than $\Delta\eta$ inferred from mantle convection has long been recognized (e.g., *Yuen et al.*, 1986; *Han et al.*, 2024). Yet, modern GIA-models continue to favor $\Delta\eta$ <10 (e.g., *Peltier*, 2004; *Peltier et al.,* 2015) with some important exceptions (e.g., $\Delta\eta$~100, *Mitrovica & Forte*, 2004; $\Delta\eta$~10-100, *Lau et al.,* 2016; $\Delta\eta$~25, *Lambeck et al.,* 2017; $\Delta\eta$~40, *Caron et al.*, 2018) and while North American uplift rates have

been interpreted to require a weak lower mantle (*Argus et al.,* 2021), such constraints are dependent on ice loading history and the assumption of radial viscosity structure. Indeed, all of the above models rely on spherical symmetry and neglect the effects of lateral variations in mantle viscosity.

Approximating the Earth's viscosity structure as a 1D-profile was necessary to make the GIA problem tractable (e.g., *Peltier,* 1974; *Cathles*, 1975). However, mantle viscosity is expected to vary in 3D from laboratory-derived olivine creep laws (e.g. *Hirth & Kohlstedt*, 2003), tectonic plate motions (*van Summeren et al*., 2012; *Becker*, 2006; *Zhong*, 2001), thermal boundary layer instabilities (*van Hunen et al.*, 2005), and lithospheric thickness variations (*Burov & Diament*, 1995; *Bellas & Zhong,* 2021). The importance of lateral viscosity variations (LVVs) to GIA has long been recognized (e.g. *Kaufmann & Wu*, 1998; *Paulson et al.*, 2005; *Latychev et al*., 2005; *A et al.*, 2013; *Sasgen et al.*, 2017) and recent studies explored a range of observational constraints and viscosity fields (e.g. *Li et al.,* 2018, 2020; *Bagge et al.,* 2021). For example, relative sea level (RSL) records in Fennoscandia are best fit by $\Delta\eta$~10, while those in North America are best fit by $\Delta\eta$~30 (*Kang et al.*, 2025; *Parang et al*., 2024; *Kuchar et al.*, 2019). Meanwhile, geodetically inferred uplift rates in North America are best-fit by $\Delta\eta$~10 in 1D-viscosity models of GIA with ICE-6G (*Argus et al*., 2021). Furthermore, different GIA observables are associated with different sensitivity to both viscosity and ice loading history (*Lau et al.,* 2018). Deformation induced by the shorter lengthscale Fennoscandian loading is sensitive to shallower mantle viscosity than North American loading (*Mitrovica,* 1996). The rate of change in Earth oblateness, $\dot{J}_2$, constrains viscosity at the largest depths but may still be regionally biased (*Kim et al.,* 2022). Thus, differences in viscosity inferred from different methods may stem from an incomplete sampling of the mantle by GIA observations.

We aim to reconcile the persistent discrepancies in bulk mantle viscosity by exploring the effects of 3D viscosity variations in models of GIA, using a range of constraints including RSL records, GNSS-observed crustal uplift, $\dot{J}_2$, and polar motion rates. We show that accounting for 3D-viscosity allows GIA models to accommodate a strong lower mantle ($\Delta\eta$~30), reconciles the discrepancy between lower mantle viscosity inferred from GIA ($\Delta\eta$~10) and mantle convection ($\Delta\eta$~30), as well as that between North American GNSS uplift ($\Delta\eta$~10) and RSL ($\Delta\eta$~30), and

improves the fit to global RSL records, $\dot{J}_2$, and polar motion in exchange for a small penalty to the GNSS-uplift misfit compared to VM5a.

Observations

We consider four types of observations: RSL records, GNSS-uplift rates, $\dot{J}_2$, and polar motion rates. For RSL, the records span North America, Fennoscandia, and the far-field (i.e., far from the ice sheets of the last glacial maximum) at 192 sites, where a timeseries of RSL at each site is derived from observations spanning thousands of years (*Peltier et al.,* 2015; *Lambeck et al.*, 2017; *Vacchi et al*., 2018; *Engelhart & Horton*, 2012; *Engelhart et al.*, 2015) (Figure S1).

For GNSS-based vertical land motion rates, we use the analyses of (i) *Hammond et al.* (2016) where uplift rates are interpolated onto a grid that spans all land, (ii) *Schumacher et al.* (2018) where non-GIA sources of vertical motion are removed, and (iii) *Argus et al.* (2021) which includes 146 campaign sites across North America.

We use $\dot{J}_2$ as estimated from satellite laser ranging data (*Loomis et al.,* 2025) and simultaneously fit annual, semi-annual, and linear terms to estimate a total mean $\dot{J}_2(1976 \leq t \leq 1991) = -3.1 \pm 0.2 \times 10^{-11}$ year^{-1}. However, for the GIA-driven component, we estimate an adjusted $\dot{J}_2 = -4.5 \pm 0.5 \times 10^{-11}$ year^{-1} by calculating the glacier mass loss contribution $\dot{J}_2 = 1.4 \times 10^{-11}$ year^{-1} between 1980 and 1992 (*Rounce et al.*, 2023) with composite error based on climate variability and tides (0.3×10^{-11} year^{-1}; *Cheng et al.,* 2013), glaciers (0.4×10^{-11} year^{-1}; *Lau et al.,* 2016), and formal error (0.2×10^{-11} year^{-1}; *Loomis et al.,* 2025).

Long term polar motion rates are based on the IERS C01 EOP timeseries from 1900-2000 (*Vondrak et al*., 2010), where $x_p = 0.55$ milliarcseconds/year and $y_p = -2.61$ milliarcseconds/year .

Methods

We employ the finite element model CitcomSVE-3.0 (*Zhong et al*., 2022; *Yuan et al.*, 2025) to compute the viscoelastic response of a self-gravitating, compressible, Maxwellian, 3D-spherical continuum including the effects of sea level change, polar- and center-of-mass-motion (for details, see the SI) to ICE-6G (122 ka to present).

Viscosity

We construct 3D-viscosity fields by scaling the seismic tomographic model S40RTS (*Ritsema et al.,* 2011) to dimensionless temperature following

$$T'(\boldsymbol{r}) = 1 - dT'(\boldsymbol{r}) \quad (1)$$

$$\mathrm{d}T'(\boldsymbol{r}) = \frac{0.035\rho_{\mathrm{PREM}}(r)}{\rho_0}\mathrm{d}v_S(\boldsymbol{r}) \quad (2)$$

where $T'(\boldsymbol{r})$ is dimensionless temperature ($T(\boldsymbol{r})' = (T(\boldsymbol{r})–T_0)/(T_1–T_0)$, $T_0 = 273$ K, $T_1 = 1573$ K), $\mathrm{d}T'(\boldsymbol{r})$ is the dimensionless temperature perturbation, $\boldsymbol{r}$ is position in 3D-spherical geometry, 0.035 is a scaling factor (e.g., *Panasyuk & Hager*, 2000; *Becker*, 2006), $\rho_{\mathrm{PREM}}(r)$ is the density profile based on PREM (*Dziewonski & Anderson*, 1981), $\rho_0 = 3300$ kg/m^3 is the reference mantle density, and $\mathrm{d}v_S(\boldsymbol{r})$ is the seismic velocity perturbation. Viscosity, $\eta(\mathbf{r})$, is estimated following

$$\eta(\boldsymbol{r}) = \eta_0(r)\exp\left(\frac{E'}{T'(\boldsymbol{r}) + T_0'} - \frac{E'}{1 + T_0'}\right), \quad (3)$$

where $\eta_0(r)$ is the reference viscosity profile, $E' = E/R(T_1–T_0)$ is the nondimensional activation energy which controls the amplitude of lateral variations in viscosity, R is the universal gas constant, and $T_0' = T_0/(T_1–T_0)$ is the nondimensional surface temperature. We ignore effects from compositional or volatile differences and use Newtonian viscosity for simplicity.

We explore the effects of 1D-radial viscosity ($E = 0$) compared to moderately ($E = 120$ kJ/mol) and strongly temperature-dependent viscosity ($E = 360$ kJ/mol), where the latter values appear appropriate for diffusion and dislocation creep rheology in olivine (e.g. *Hirth & Kohlstedt*, 2003; *van Hunen et al.*, 2005; *Becker*, 2006). The reference viscosity profile VM5a has a weak lower mantle ($\Delta\eta$=6.4) compared to EM1 ($\Delta\eta$=31.5), where EM1 is consistent with mantle convection studies and produces a good fit to North American RSL (*Kang et al.,* 2025). We explore six cases, setting $\eta_0(r)$ equal to VM5a or EM1 and E equal to zero (*WeakLM_NoLVVs* and *StrongLM_NoLVVs*, respectively), 120 kJ/mol (*WeakLM_ModerateLVVs* and *StrongLM_ModerateLVVs*), or 360 kJ/mol (*WeakLM_StrongLVVs* and *StrongLM_StrongLVVs*) (Figure 1). Note the Haskell constraint degenerates from radial to volumetric for 3D viscosity.

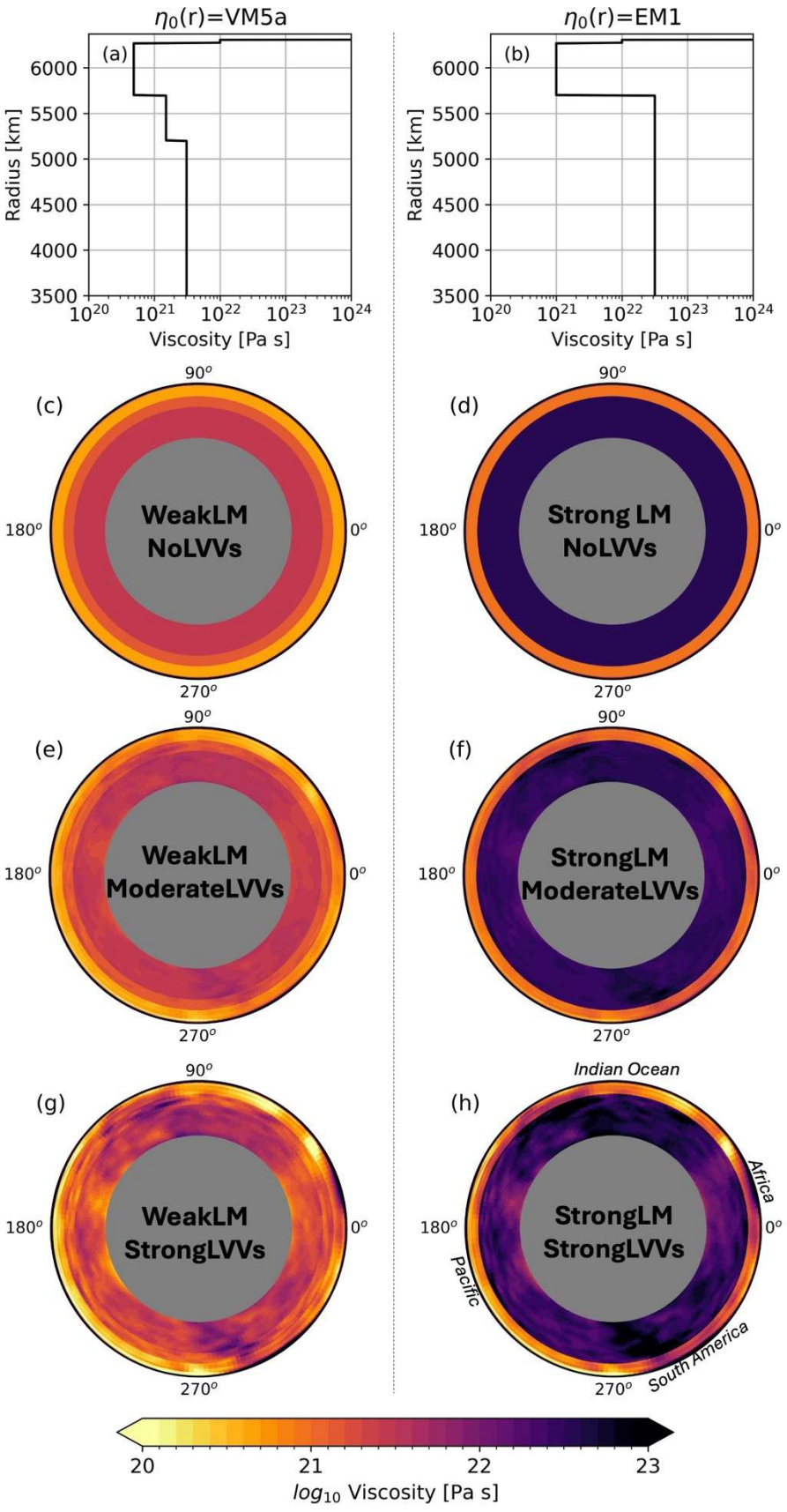
η_0(r)=VM5a
η_0(r)=EM1
(a)
(b)
Radius [km]
6000
5500
5000
4500
4000
3500
10^{20}
10^{21}
10^{22}
10^{23}
10^{24}
Viscosity [Pa s]
(c)
WeakLM
NoLVVs
(d)
Strong LM
NoLVVs
(e)
WeakLM
ModerateLVVs
(f)
StrongLM
ModerateLVVs
(g)
WeakLM
StrongLVVs
(h)
StrongLM
StrongLVVs
90°
180°
0°
270°
Indian Ocean
Africa
Pacific
South America
20
21
22
23
log_{10} Viscosity [Pa s]

167

Figure 1. *The reference viscosity profiles (a-b), and an equatorial slice of the 3D-viscosity fields based thereupon for increasing activation energy, E, which controls the amplitude of LVVs scaled from seismic tomography: E = 0 kJ/mol (c-d), E = 120 kJ/mol (e-f), and E = 360 kJ/mol (g-h).*

Misfits

We compute the root of the mean squared error (RMSE) to the RSL record at each site, *i,* as

$$RMSE_i^{(RSL)} = \sqrt{\frac{1}{N_t^{(i)}} \sum_{j=1}^{N_t^{(i)}} \left(\frac{RSL_i^{(obs)}(t_j) - RSL_i^{(pred)}(t_j)}{\sigma_i^{(obs)}(t_j)} \right)^2} \quad (4)$$

and the misfit to the set of RSL records

$$RMSE^{(RSL)} = \frac{1}{N_{sites}} \sum_{i=1}^{N_{sites}} RMSE_i^{(RSL)} \quad (5)$$

where $N_t^{(i)}$ is the number of data points in the RSL timeseries at each site *i*, $RSL_i^{(obs)}(t_j)$ is the observed RSL at site *i* and time *j*, $RSL_i^{(pred)}(t_j)$ is the predicted RSL at site *i* and time *j*, and $\sigma_i^{(obs)}(t_j)$ is the error in $RSL_i^{(obs)}(t_j)$.

We compute the misfit to GNSS-uplift rates as RMSE based on a regular grid to avoid overweighting densely sampled regions. Observations are interpolated onto a grid where any grid point with distance > 100 km from a GNSS-site is masked (i.e., assigned NaN). Then,

$$RMSE^{(VLM)} = \sqrt{\frac{1}{A} \int \left(v_z^{(obs)}(\theta, \phi) - v_z^{(pred)}(\theta, \phi) \right)^2 dA} \quad (6)$$

where A is the total area of the unmasked grid region, θ is latitude, and ϕ is longitude, and dA is the area increment.

Results

Global Misfits

The misfit to RSL records is reduced by ~40% when the reference viscosity is changed from VM5a (weak lower mantle) to EM1 (strong lower mantle), regardless of the strength of LVVs (Figure 2; Table S1). If LVVs are zero or moderate, the GNSS-misfit is increased by 10-20% for a strong vs. weak lower mantle (Figure 2; Table S2; Table S3). However, if LVVs are strong, changing the reference viscosity from VM5a to EM1 has no effect on the misfit to GNSS-uplift (compare *WeakLM_StrongLVVs* to *StrongLM_StrongLVVs*). Therefore, increasing lower mantle viscosity and implementing strong LVVs (*StrongLM_StrongLVVs*) reduces the $RMSE^{(RSL)}$ by ~40%, while the misfit to GNSS-uplift is unchanged compared to *WeakLM_StrongLVVs*, or slightly increased (~5%) compared to *WeakLM_NoLVVs* (i.e., VM5a). The reduction in the misfit to RSL records is ~50% if we do not normalize by error in eq. (4) (Table S1).

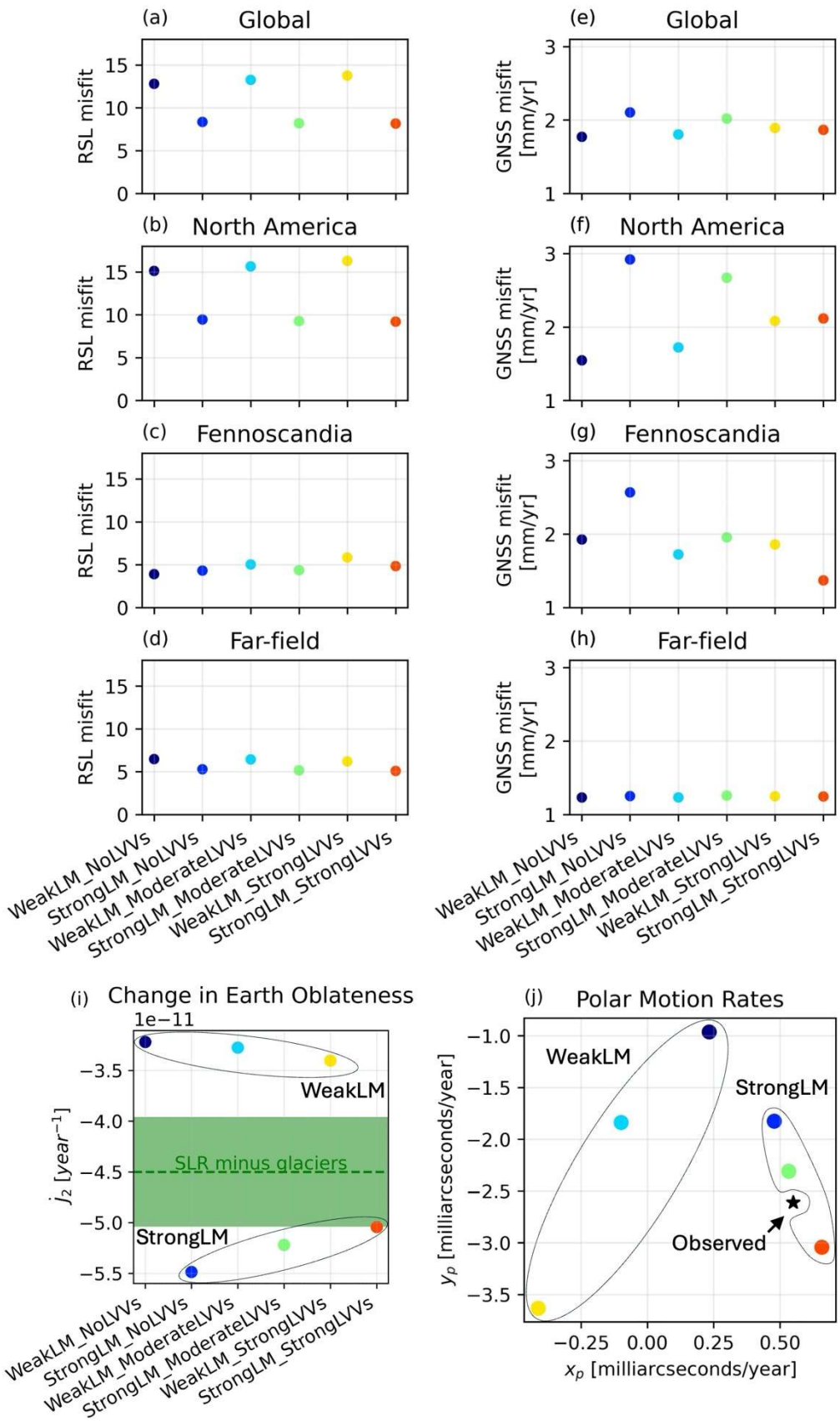
(a) Global
(b) North America
(c) Fennoscandia
(d) Far-field
RSL misfit
(e) Global
(f) North America
(g) Fennoscandia
(h) Far-field
GNSS misfit [mm/yr]
WeakLM_NoLVVs
StrongLM_NoLVVs
WeakLM_ModerateLVVs
StrongLM_ModerateLVVs
WeakLM_StrongLVVs
StrongLM_StrongLVVs
(i) Change in Earth Oblateness
1e−11
$\dot{J}_2$ [year^{-1}]
WeakLM
SLR minus glaciers
StrongLM
(j) Polar Motion Rates
WeakLM
StrongLM
Observed
y_p [milliarcseconds/year]
x_p [milliarcseconds/year]

199

Figure 2. *Misfits to RSL records (a-d), GNSS-uplift (e-h),* $\dot{J}_2$ *(i), and polar motion rates (j). Our new preferred 3D-viscosity model of GIA is* StrongLM_StrongLVVs *(red dot).*

This is significant because GIA models that neglect LVVs predict uplift rates that are much larger than observed when a strong lower mantle is implemented, especially in North America (e.g., 2 times larger; *Argus et al.*, 2021) and have long been interpreted to preclude a strong lower mantle (e.g., *Cathles*, 1975). However, we show here that *StrongLM_StrongLVVs* reproduces global GNSS-uplift nearly equally well with just a 5% penalty compared to models with a weak lower mantle. In the regional results presented below, we show that lateral variations in viscosity have a strong influence on the predicted uplift rates, especially in North America.

North America

In North America, the relationship between $\eta_0(r)$ and the misfit to RSL records is the same as the global average: the misfit to RSL records is reduced by ~40% for $\eta_0(r)$ = EM1 (strong lower mantle) compared to VM5a (weak lower mantle), regardless of the strength of LVVs (Figure 2; Figure S2-S6; Table S4). The relationship between the GNSS misfit and lower mantle viscosity is similar to the global average, in that strong LVVs make the GNSS misfit insensitive to lower mantle viscosity, but penalties associated with accounting for LVVs arise. Considering cases with a weak lower mantle only ($\eta_0(r)$ = VM5a), accounting for LVVs in North America results in a 10-30% increase in the GNSS misfit, compared to 5% in the global average. This may be a consequence of the coupled solution for ICE-6G with VM5a. If LVVs are strong and $\eta_0(r)$=EM1 (the preferred case globally, *StrongLM_StrongLVVs*), then the GNSS misfit is (i) equal to that of *WeakLM_StrongLVVs*, (ii) increases by 20% compared to *WeakLM_ModerateLVVs*, and (iii) increases by 35% compared to *WeakLM_NoLVVs*. Maps of the North American uplift pattern from GNSS and predictions from *WeakLM_NoLVVs, WeakLM_StrongLVVs, StrongLM_StrongLVVs* are presented in Figure 3.

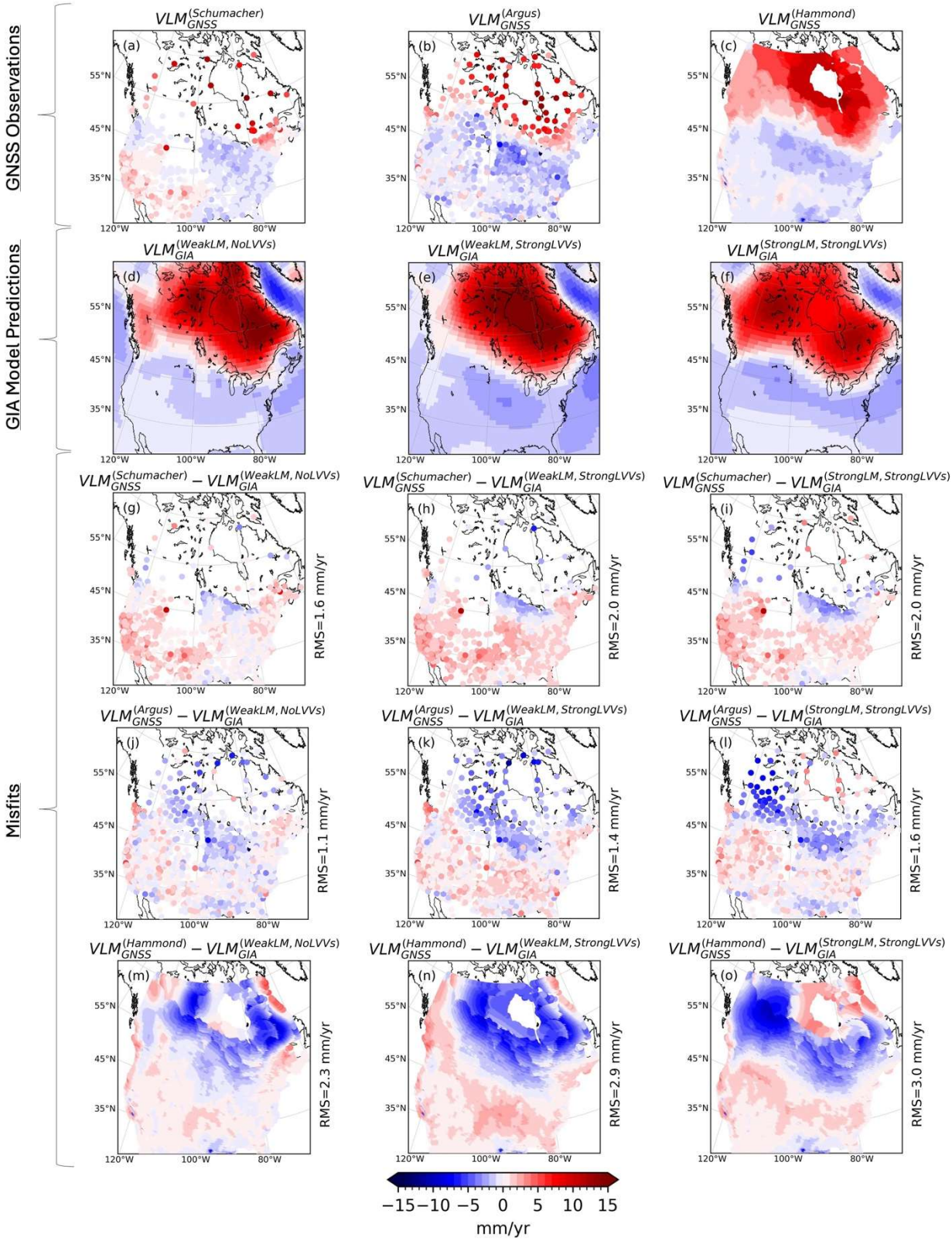
GNSS Observations
GIA Model Predictions
Misfits
$VLM^{(Schumacher)}_{GNSS}$
$VLM^{(Argus)}_{GNSS}$
$VLM^{(Hammond)}_{GNSS}$
$VLM^{(WeakLM,\,NoLVVs)}_{GIA}$
$VLM^{(WeakLM,\,StrongLVVs)}_{GIA}$
$VLM^{(StrongLM,\,StrongLVVs)}_{GIA}$
$VLM^{(Schumacher)}_{GNSS} - VLM^{(WeakLM,\,NoLVVs)}_{GIA}$
$VLM^{(Schumacher)}_{GNSS} - VLM^{(WeakLM,\,StrongLVVs)}_{GIA}$
$VLM^{(Schumacher)}_{GNSS} - VLM^{(StrongLM,\,StrongLVVs)}_{GIA}$
$VLM^{(Argus)}_{GNSS} - VLM^{(WeakLM,\,NoLVVs)}_{GIA}$
$VLM^{(Argus)}_{GNSS} - VLM^{(WeakLM,\,StrongLVVs)}_{GIA}$
$VLM^{(Argus)}_{GNSS} - VLM^{(StrongLM,\,StrongLVVs)}_{GIA}$
$VLM^{(Hammond)}_{GNSS} - VLM^{(WeakLM,\,NoLVVs)}_{GIA}$
$VLM^{(Hammond)}_{GNSS} - VLM^{(WeakLM,\,StrongLVVs)}_{GIA}$
$VLM^{(Hammond)}_{GNSS} - VLM^{(StrongLM,\,StrongLVVs)}_{GIA}$
(a)
(b)
(c)
(d)
(e)
(f)
(g)
(h)
(i)
(j)
(k)
(l)
(m)
(n)
(o)
RMS=1.6 mm/yr
RMS=2.0 mm/yr
RMS=2.0 mm/yr
RMS=1.1 mm/yr
RMS=1.4 mm/yr
RMS=1.6 mm/yr
RMS=2.3 mm/yr
RMS=2.9 mm/yr
RMS=3.0 mm/yr
55°N
45°N
35°N
120°W
100°W
80°W
−15 −10 −5 0 5 10 15
mm/yr

224

Figure 3. *North American uplift rates from (a-c) three GNSS datasets, (d-f) models* WeakLM_NoLVVs, WeakLM_StrongLVVs, StrongLM_StrongLVVs*, and (g-o) the corresponding misfits computed on a point-by-point basis.*

Compared to the global average, the penalty to the GNSS misfit for increasing lower mantle viscosity is greater in North America. Nonetheless, the penalty for a strong lower mantle is significantly reduced by accounting for LVVs (*StrongLM_StrongLVVs* vs. *WeakLM_StrongLVVs*; Figure 3) compared to 1D-viscosity (*StrongLM_NoLVVs* vs. *WeakLM_NoLVVs*; Figure 2f). Furthermore, it is not clear that the 35% increase in GNSS misfit of *StrongLM_StrongLVVs* compared to *WeakLM_NoLVVs* is the most representative comparison, since that latter neglects LVVs. Rather, comparing *StrongLM_StrongLVVs* with *WeakLM_ModerateLVVs* and *WeakLM_StrongLVVs* yields a 0-20% increase in the misfit. In combination with the 40% reduction in the RSL misfit, this leads us to conclude that *StrongLM_StrongLVVs* is the preferred model on a regional basis in North America despite larger tradeoff with GNSS-uplift than the global average.

The misfit to North American uplift is highly sensitive to lower mantle viscosity when the lithosphere is thinner (e.g., *WeakLM_NoLVVs, WeakLM_ModerateLVVs, StrongLM_NoLVVs,* and *StrongLM_ModerateLVVs*) but becomes insensitive to lower mantle viscosity when the lithosphere is thicker (e.g., *WeakLM_StrongLVVs* and *StrongLM_StrongLVVs*). To understand this result, we present horizontal averages and vertical transects of 3D-viscosity which show that for *WeakLM_StrongLVVs* and *StrongLM_StrongLVVs*, the average viscosity is ~equal to the reference viscosity profiles (cf. *WeakLM_NoLVVs* and *StrongLM_NoLVVs*) at depths larger than ~200 km, but converge at shallow depths < 200 km to a much stronger viscosity profile (Figure 4). This indicates that lithospheric thickness has a significant impact on uplift and reduces sensitivity of the misfit to lower mantle viscosity (Figure 4, Figure S7; cf. *Lau et al.* 2018). However, differences in lower mantle viscosity produce differences in the pattern of uplift (Figure 3) and mantle strain rate (Figure 4) even when the lithosphere is thick. For example, *WeakLM_StrongLVVs* exhibits a single maximum center of uplift around the Hudson Bay (Figure 3e), while *StrongLM_StrongLVVs* exhibits two maximum uplift centers in Quebec and Northwestern Canada (Figure 3f). The maximum uplift center in Northwestern Canada produces

most of the misfit in *StrongLM_StrongLVVs* (Figure 3o) and is sparsely sampled by GNSS observations (Figure 3a), highlighting the need for additional permanent stations in this region.

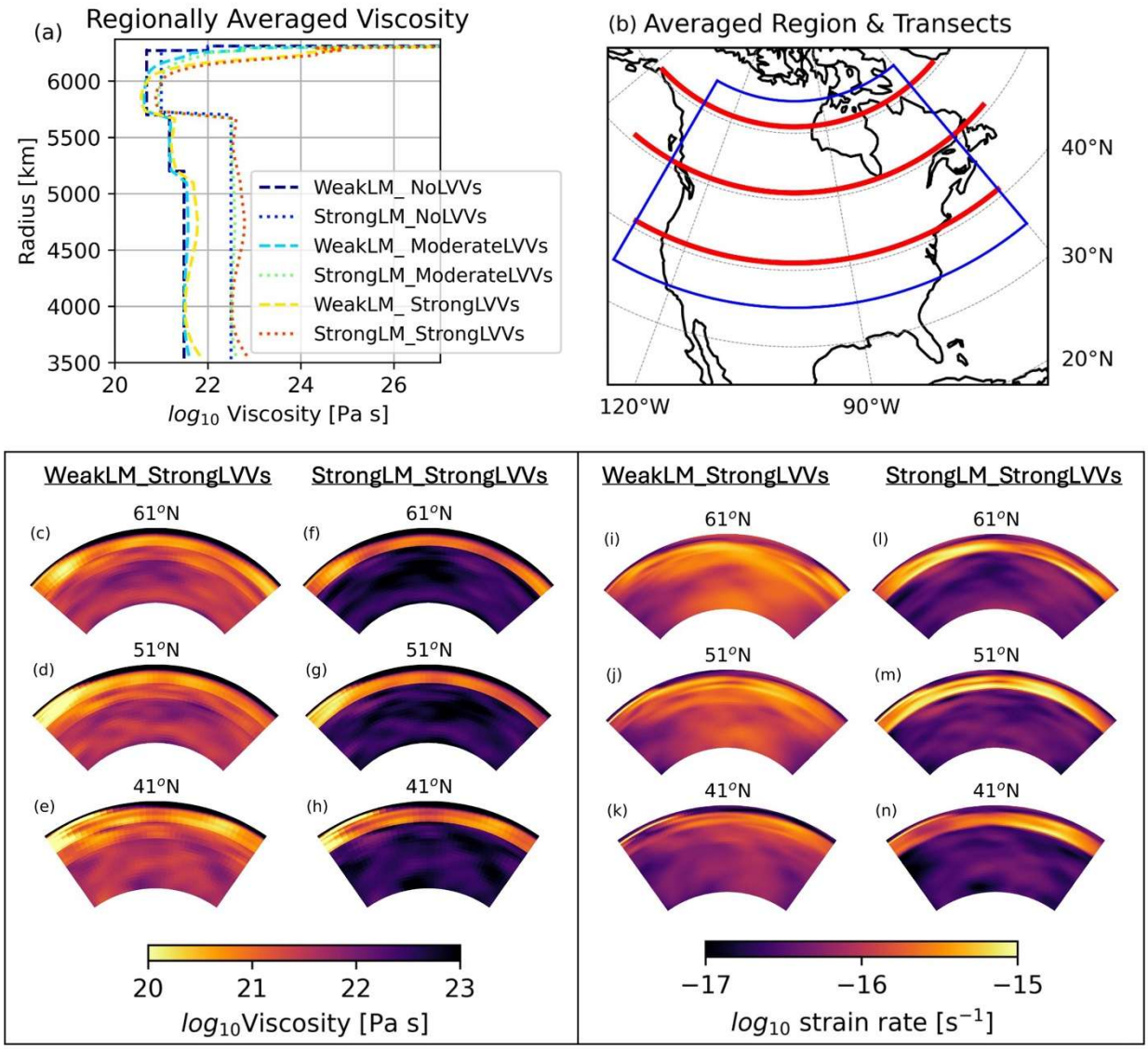

Figure 4. *(a) Laterally averaged viscosity in the region outlined in blue in (b), as well as three cross-sections of mantle viscosity (c-h) and strain rate (i-n) shown by red curves in (b).* WeakLM_StrongLVVs *and* StrongLM_StrongLVVs *reproduce North American GNSS-uplift equally well despite different lower mantle viscosities.*

Our results imply that the disagreement on lower mantle viscosity from mantle convection and GIA may be resolved by considering 3D-viscosity in models of GIA. Predictions from GIA models that neglect LVVs suggest the lower mantle cannot be strong because North American

uplift rates preclude it (*Argus et al.*, 2021). However, our results show that accounting for 3D-viscosity (in particular, lithospheric thickness variations) makes a strong lower mantle viable in terms of reproducing the observed uplift rates in North America, while contributing a greater reduction to the RSL misfit.

Previous efforts to reconcile mantle viscosity from studies of mantle convection and GIA performed joint inversions for 1D-viscosity (*Mitrovica & Forte*, 2004) and we find this profile produces a smaller reduction in the misfit to RSL records (~15%) and a greater increase in the misfit to GNSS-uplift (~45%) compared to our preferred 3D model *StrongLM_StrongLVVs*. The 1D-viscosity profile from *Lau et al.* (2016) reproduces RSL records and GNSS-uplift similarly to *WeakLM_NoLVVs*, and that from *Caron et al.* (2018) performs similarly to *StrongLM_NoLVVs*. Within the confines of ice loading from ICE-6G, this substantiates the importance of 3D-viscosity, particularly lithospheric thickness variations, in reconciling viscosity inferred from GIA and mantle convection studies. Misfits are similar to *StrongLM_NoLVVs* if the viscosity contrast is increased to $\Delta\eta$=50, with some degradation if $\Delta\eta$=100 particularly in $\dot{J}_2$ and polar motion, although the latter improves mantle convection model fits to the long-wavelength geoid (*Mao & Zhong*, 2021; Figure S8).

Fennoscandia

In Fennoscandia, the RSL misfit based on 12 sites is not particularly sensitive to changes in lower mantle viscosity, which is not unexpected given the short lengthscale of this region. The RSL misfit decreases by 10-20% for a strong lower mantle ($\eta_0(r)$ = EM1) compared to a weak lower mantle ($\eta_0(r)$ = VM5a) when LVVs are moderate or strong (Figure 2). While the minimum RSL misfit is produced by *WeakLM_NoLVVs* (e.g., ~25% smaller than *StrongLM_StrongLVVs*), the misfit values in Fennoscandia are substantially smaller than global and North American results, indicating that the RSL records are quite well-fit by all viscosity structures considered herein (Figure 2; Figure S9). The GNSS misfit is minimized by *StrongLM_StrongLVVs* which produces a 30% reduction compared to *WeakLM_NoLVVs*, and a ~25% decrease compared to *WeakLM_StrongLVVs*, suggesting increased T_e increases sensitivity to lower mantle viscosity (Figure S7; cf. *Lau et al.*, 2018).

Far-field

In the far-field, the RSL misfit based on 36 sites decreases by ~20% for a strong vs. weak lower mantle, with *StrongLM_StrongLVVs* producing the best-fit (Figure S10). The GNSS residuals do not change appreciably across the cases considered, where the misfit of *StrongLM_StrongLVVs* is approximately equal (<10% difference) to that of *WeakLM_NoLVVs* (Figure 2).

Oblateness

In general, cases with a weak lower mantle ($\eta_0(r)$ = VM5a) produce $\dot{J}_2 \cong -3 \times 10^{-11}$ and those with a strong lower mantle ($\eta_0(r)$ = EM1) produce $\dot{J}_2 \cong -5 \times 10^{-11}$ year^{-1} (Figure 2). Compared to the target $\dot{J}_2 = -4.5 \pm 0.2 \times 10^{-11}$ year^{-1}, the latter group performs better and only *StrongLM_StrongLVVs* is within error of the observed estimate.

Polar Motion

Polar motion rates are best reproduced by models with a strong lower mantle. The best-fit case is *StrongLM_ModerateLVVs* while *StrongLM_StrongLVVs* is second-best with 75% reduction in the misfit compared to *WeakLM_NoLVVs* (Figure 2).

Discussion

The ice loading model ICE-6G combined with 1D-viscosity profile VM5a is a widely accepted global model of GIA because it fits a wealth of data, including global RSL records, GNSS-uplift, $\dot{J}_2$, and geologic constraints on the lateral extent of ice sheets through time. However, there is an equally compelling collection of observations that cannot be reconciled with the lower mantle viscosity of VM5a, including the static geoid and tectonic plate motions, which indicate a more significant increase in viscosity toward the lower mantle.

Our results show that accounting for 3D-viscosity in models of GIA can simultaneously (i) improve the fit to global RSL records in exchange for a small penalty on the GNSS-uplift residuals, and (ii) reconcile the longstanding conflict with mantle convection constraints on lower mantle viscosity. In particular, the GNSS-uplift rates in North America cannot be reproduced in 1D-models of GIA with a strong lower mantle and ICE-6G, regardless of lithospheric thickness (Figure S11). However, we show that GNSS-uplift rates are fit equally well by a strong vs. weak lower mantle when LVVs are strong.

Recent GIA studies already showed that the regional fit to RSL records in North America is improved when lower mantle viscosity is strong (e.g., $\Delta\eta \sim 30$) based on 1D- (*Kang et al.*, 2025) and 3D-viscosity in GIA models (*Kuchar et al.*, 2019) but GNSS-uplift was not considered. It has also been shown with 1D-viscosity models of GIA that RSL records along the Northeast coast of North America prefer a strong lower mantle while those around Hudson Bay prefer a weak lower mantle (*Parang et al*., 2024). While *Bagge et al.* (2021) considered reference viscosities consistent with geoid modeling only, *Li et al.* (2018, 2020) considered reference viscosity equal to VM5a only.

Our contribution here is thus to (i) compute the GIA response with LVVs based on seismic tomography, (ii) consider the reference viscosity profiles recommended by both mantle convection and GIA studies, (iii) vary the strength of LVVs, and (iv) compute global misfits to RSL records, GNSS-uplift, $\dot{J}_2$, and polar motion. We show that an increased lower mantle viscosity consistent with mantle convection studies improves the fit to RSL records and fits GNSS-uplift equally well if LVVs are strong. While there is some degradation in the fit to GNSS-uplift rates in North America compared to 1D-viscosity profile VM5a, this is offset by improvement in Fennoscandia, and we suggest that additional model refinement (e.g., ice history, a weak asthenosphere) may mitigate this tradeoff. Our new preferred model is case *StrongLM_StrongLVVs* loaded by ICE-6G, which also improves the fit to $\dot{J}_2$ and polar motion.

The implications of what may be a step toward an updated global reference GIA model are broad. For example, it may have a significant impact on the global mean terrestrial water storage trend (*Rodell et al.,* 2024), the global mean sea level budget (*Barnoud et al.,* 2023), the pole tide correction (*Wahr et al*., 2015), and the hydrological component of $\dot{J}_2$ (*Nerem & Wahr*, 2011). We did not consider variations in the ice loading history ICE-6G. While the lateral extent of ice sheets is constrained by geological observations, the ice height within these margins is typically varied with the 1D-viscosity structure in GIA models. Advances in the ice loading history may impact the results presented herein. We also considered only one seismic tomographic model, S40RTS, but we suggest that the results will be broadly similar for others given similar long-wavelength features.

Conclusions

Accounting for lateral viscosity variations in GIA models reconciles two discrepancies: (i) GIA appears to require a weak lower mantle to fit global RSL records, GNSS uplift, and $\dot{J}_2$, while mantle convection constraints require a strong lower mantle to reproduce the static geoid and slab sinking rates; (ii) 1D-viscosity models of GIA require a strong lower mantle to best-fit RSL records in North America, but a weak lower mantle to fit the GNSS uplift rates. Compared to the 1D reference viscosity profile VM5a ($\Delta\eta \sim 10$), the fit to RSL records, $\dot{J}_2$, and polar motion rates is substantially improved in exchange for a small penalty in the misfit to GNSS-uplift when lateral viscosity variations (LVVs) and a strong lower mantle compatible with mantle convection constraints ($\Delta\eta \sim 30$) are considered. Regionally, the misfit to GNSS-uplift is degraded in North America and improved in Fennoscandia compared to VM5a, but this is less significant compared to VM5a with moderate to strong LVVs, which may be a more representative rheological Earth structure. Our preferred model with LVVs and a strong lower mantle may be a step toward an updated global reference with broad implications for the interactions of the solid Earth, hydrosphere, and cryosphere including for the study of sea level.

Acknowledgements

Many thanks to two anonymous reviewers for thoughtful and constructive feedback, and to Evan Wilson and Khosro Ghobadi-Far for help with the polar motion data. ABM and RSN were supported by the NASA Sea Level Change Team under Grant 80NSSC24K1651. KK and TWB were partially supported by NSF EAR 2045292 and 19214743, and KK acknowledges support from the Jackson School for Geosciences at UT Austin's post-doctoral program. Computations were performed on the LS6 and Frontera computers of the Texas Advanced Computing Center.

Conflict of Interest

The authors declare no conflict of interest relevant to this study.

Open Research

The RSL records used to constrain the models are compiled together and available for download, along with the gridded present-day rate maps associated with our new preferred 3D viscosity model of GIA in terms of uplift, the geoid, and RSL (*Bellas-Manley*, 2025 ; *Peltier et al.,* 2015; *Lambeck et al.*, 2017; *Vacchi et al*., 2018; *Engelhart & Horton*, 2012; *Engelhart et al.*, 2015; https://doi.org/10.5281/zenodo.17516836). The GNSS-uplift (*Argus et al*., 2021; *Hammond et*

al., 2016; *Schumacher et al*., 2018), J_2 (*Loomis et al.,* 2025) and polar motion timeseries (*Vondrak et al*., 2010; https://hpiers.obspm.fr/iers/eop/eopc01/) are publicly available for download from their respective references, as is the finite element model CitcomSVE-3.0 (*Yuan & Zhong*, 2024) and the ICE-6G ice loading history (*Peltier et al*., 2015; https://www.atmosp.physics.utoronto.ca/~peltier/data.php).

References

A, G. R., Wahr, J., & Zhong, S. (2013). Computations of the viscoelastic response of a 3-D compressible earth to surface loading: An application to glacial isostatic adjustment in Antarctica and Canada. Geophysical Journal International, 192(2), 557–572. https://doi.org/10.1093/gji/ggs030

Argus, D. F., Peltier, W. R., Blewitt, G., & Kreemer, C. (2021). The Viscosity of the top third of the lower mantle estimated using GPS, GRACE, and relative sea level measurements of glacial isostatic adjustment [Dataset]. Journal of Geophysical Research: Solid Earth, 126, e2020JB021537. https://doi.org/10.1029/2020JB021537

Argus, D. F., W. R. Peltier, R. Drummond, A. W. Moore, The Antarctica component of postglacial rebound model ICE-6G_C (VM5a) based on GPS positioning, exposure age dating of ice thicknesses, and relative sea level histories, *Geophysical Journal International*, Volume 198, Issue 1, July, 2014, Pages 537–563, https://doi.org/10.1093/gji/ggu140

Bagge, M., Klemann, V., Steinberger, B., Latinović, M. and Thomas, M., 2021. Glacial-isostatic adjustment models using geodynamically constrained 3D Earth structures. *Geochemistry, Geophysics, Geosystems*, *22*(11), p.e2021GC009853.

Barnoud, A., Pfeffer, J., Cazenave, A., Fraudeau, R., Rousseau, V., and Ablain, M.: Revisiting the global mean ocean mass budget over 2005–2020, Ocean Sci., 19, 321–334, https://doi.org/10.5194/os-19-321-2023, 2023.

Becker, T. W., On the effect of temperature and strain-rate dependent viscosity on global mantle flow, net rotation, and plate-driving forces, *Geophysical Journal International*, Volume 167, Issue 2, November 2006, Pages 943–957, https://doi.org/10.1111/j.1365-246X.2006.03172.x

Beckley, B. D., Callahan, P. S., Hancock, D. W., Mitchum, G. T., & Ray, R. D. (2017). On the "cal-mode" correction to TOPEX satellite altimetry and its effect on the global mean sea level time series. *Journal of Geophysical Research: Oceans*, 122, 8371–8384. https://doi.org/10.1002/2017JC013090

Bellas-Manley, A., & Royden, L. (2024). Basal mantle flow over LLSVPs explains differences in Pacific and Indo-Atlantic hotspot motions. Journal of Geophysical Research: Solid Earth, 129, e2023JB027636. https://doi. org/10.1029/2023JB027636

Bellas-Manley, A. (2025). Outputs and observations used to constrain models in Bellas-Manley et al. (2026) GRL [Dataset]. Zenodo. https://doi.org/10.5281/zenodo.17516836

Bellas, A., & Zhong, S. (2021). Effects of a weak lower crust on the flexure of continental lithosphere. Journal of Geophysical Research: Solid Earth, 126, e2021JB022678. https://doi.org/10.1029/2021JB022678

Berends, C. J., Köhler, P., Lourens, L. J., & van de Wal, R. S. W. (2021). On the cause of the mid-Pleistocene transition. Reviews of Geophysics, 59, e2020RG000727. https://doi.org/10.1029/2020RG000727

Bunge, HP., Richards, M. & Baumgardner, J. Effect of depth-dependent viscosity on the planform of mantle convection. *Nature* 379, 436–438 (1996). https://doi.org/10.1038/379436a0

Burov, E. B., and M. Diament (1995), The effective elastic thickness (T_e) of continental lithosphere: What does it really mean? *J. Geophys. Res.*, 100(B3), 3905–3927, doi:10.1029/94JB02770.

Cathles, L. M. 1975. *The viscosity of the earth's mantle.* Princeton, NJ: Princeton University Press.

Caron, L., Ivins, E. R., Larour, E., Adhikari, S., Nilsson, J., & Blewitt, G. (2018). GIA model statistics for GRACE hydrology, cryosphere, and ocean science. Geophysical Research Letters, 45, 2203–2212. https://doi.org/10.1002/2017GL076644

Dziewonski, A. M. & Anderson, D. L. Preliminary reference Earth model. Phys. Earth Planet. Inter. 25, 297–356 (1981).

Engelhart, S. E., & Horton, B. P. (2012). Holocene sea level database for the Atlantic coast of the United States [dataset]. Quaternary Science Reviews, 54, 12–25. https://doi.org/10.1016/j.quascirev.2011.09.013

436 Engelhart, S. E., Vacchi, M., Horton, B. P., Nelson, A. R., & Kopp, R. E. (2015). A sea-level
437 database for the Pacific coast of central North America [Dataset]. Quaternary Science Reviews,
438 113, 78–92. https://doi.org/10.1016/j.quascirev.2014.12.001

439 Gomez, N., Yousefi, M., Pollard, D., DeConto, R. M., Sadai, S., Lloyd, A., Nyblade, A.,
440 Wiens, D. A., Aster, R. C., and Wilson, T, The influence of realistic 3D mantle viscosity on
441 Antarctica's contribution to future global sea levels. Sci. Adv.10, eadn1470 (2024).
442 DOI:10.1126/sciadv.adn1470

443 Hager, B. H. (1984), Subducted slabs and the geoid: Constraints on mantle rheology and flow, *J.*
444 *Geophys. Res.*, 89(B7), 6003–6015, doi:10.1029/JB089iB07p06003.

445 Hammond, W.C., G. Blewitt, C. Kreemer, 2016, GPS Imaging of vertical land motion in
446 California and Nevada: Implications for Sierra Nevada uplift [Dataset], Journal of Geophysical
447 Research - Solid Earth, 121(10), p. 7681-7703, https://doi.org/10.1002/2016JB013458.

448 Han, H. K., Gomez, N., Pollard, D., & DeConto, R. (2021). Modeling Northern Hemispheric ice
449 sheet dynamics, sea level change, and solid Earth deformation through the last glacial cycle.
450 Journal of Geophysical Research: Earth Surface, 126, e2020JF006040.
451 https://doi.org/10.1029/2020JF006040

452 Han, S., T. Yuan, W. Mao, S. Zhong (2024), The persisting conundrum of mantle viscosity
453 inferred from mantle convection and glacial isostatic adjustment processes, Earth and Planetary
454 Science Letters, Volume 648, 119069, ISSN 0012-821X.

455 Haskell, N. A., The motion of a fluid under a surface load, 1, *Physics*, 6, 265–269, 1935.

456 Hassan, R., Müller, R., Gurnis, M. *et al.* A rapid burst in hotspot motion through the interaction
457 of tectonics and deep mantle flow. *Nature* 533, 239–242 (2016).
458 https://doi.org/10.1038/nature17422

459 Hirth, G., and D. L. Kohlstedt (2003), Rheology of the upper mantle and the mantle wedge: A
460 view from the experimentalists, in Inside the Subduction Factory, Geophysical Monograph, vol.
461 138, edited by J. Eiler, pp. 83–105, AGU, Washington, D. C.

462 Houriez, L., Larour, E., Caron, L., Schlegel, N.-J., Adhikari, S., Ivins, E., Pelle, T., Seroussi, H.,
463 Darve, E., and Fischer, M.: Reinforced ridges in Thwaites Glacier yield insights into resolution
464 requirements for coupled ice sheet and solid Earth models, The Cryosphere, 19, 4355–4372,
465 https://doi.org/10.5194/tc-19-4355-2025, 2025.

466 Kang, K., Yuan, T., & Zhong, S. (2025). Constraints of relative sea level change on the mantle
467 viscosity and the Late Pleistocene deglaciation history. Journal of Geophysical Research: Solid
468 Earth, 130, e2024JB030216. https://doi.org/10.1029/2024JB030216

469 Kaufmann, G. & Wu, P. (1998). Lateral asthenospheric viscosity variations and postglacial
470 rebound: a case study for the Barents Sea. Geophys. Res. Lett., 25, 1963–1966.

471 Kim, A. J., Crawford, O., Al-Attar, D., Lau, H. C. P., Mitrovica, J. X., & Latychev, K. (2022). Ice
472 age effects on the satellite-derived j˙ 2 datum: Mapping the sensitivity to 3d variations in mantle
473 viscosity. Earth and Planetary Science Letters, 581, 117372.

474 King, S. D. (1995). Radial models of mantle viscosity: Results from a genetic algorithm.
475 Geophys. J. Int., 122, 725–734.

476 Kuchar, J., G. Milne, K. Latychev, The importance of lateral Earth structure for North American
477 glacial isostatic adjustment, Earth and Planetary Science Letters, Volume 512, 2019, Pages 236-
478 245, ISSN 0012-821X, https://doi.org/10.1016/j.epsl.2019.01.046.

479 Lambeck, K., Purcell, A., & Zhao, S. (2017). The North American Late Wisconsin ice sheet and
480 mantle viscosity from glacial rebound analyses [dataset]. Quaternary Science Reviews, 158,
481 172–210. https://doi.org/10.1016/j.quascirev.2016.11.033

482 Landerer, F. W., Flechtner, F. M., Save, H., Webb, F. H., Bandikova, T., Bertiger, W. I., et al.
483 (2020). Extending the global mass change data record: GRACE Follow-On instrument and
484 science data performance. Geophysical Research Letters, 47,
485 e2020GL088306. https://doi.org/10.1029/2020GL088306

486 Latychev, K., Mitrovica, J. X., Tamisiea, M. E., Tromp, J., Christara, C. C., & Moucha, R.
487 (2005). GIA-induced secular variations in the Earth's long wavelength gravity field: Influence of
488 3-D viscosity variations. Earth Planet. Sci. Lett., 240, 322–327.

Lau, H. C. P., J. X. Mitrovica, J. Austermann, O. Crawford, D. Al-Attar, and K. Latychev (2016), Inferences of mantle viscosity based on ice age data sets: Radial structure, J. Geophys. Res. Solid Earth, 121, 6991–7012, doi:10.1002/2016JB013043.

Lau, N., Borsa, A. A., & Becker, T. W. (2020). Present-day crustal vertical velocity field for the contiguous United States. *Journal of Geophysical Research: Solid Earth*, 125, e2020JB020066. https://doi.org/10.1029/2020JB020066

Li, T., Wu, P., Steffen, H. and Wang, H., 2018. In search of laterally heterogeneous viscosity models of glacial isostatic adjustment with the ICE-6G_C global ice history model. *Geophysical Journal International*, *214*(2), pp.1191-1205.

Li, T., Wu, P., Wang, H., Steffen, H., Khan, N.S., Engelhart, S.E., Vacchi, M., Shaw, T.A., Peltier, W.R. and Horton, B.P., 2020. Uncertainties of glacial isostatic adjustment model predictions in North America associated with 3D structure. *Geophysical Research Letters*, *47*(10), p.e2020GL087944.

Li, Z.X, S. Zhong, Supercontinent–superplume coupling, true polar wander and plume mobility: Plate dominance in whole-mantle tectonics, Physics of the Earth and Planetary Interiors, Volume 176, Issues 3–4, 2009, Pages 143-156, ISSN 0031-9201, https://doi.org/10.1016/j.pepi.2009.05.004.

Lithgow-Bertelloni, C., and M. A. Richards (1998), The dynamics of Cenozoic and Mesozoic plate motions, *Rev. Geophys.*, 36(1), 27–78, doi:10.1029/97RG02282.

Loomis, B. D., Sabaka, T. J., Rachlin, K. E., Croteau, M. J., Lemoine, F. G., Nerem, R. S., & Bellas-Manley, A. (2025). Optimized J2 recovery for multi-decadal geophysical studies [Dataset]. Geophysical Research Letters, 52, e2024GL114472. https://doi.org/10.1029/2024GL114472

Mao, W., & Zhong, S. (2019). Controls on global mantle convective structures and their comparison with seismic models. Journal of Geophysical Research: Solid Earth, 124, 9345–9372. https://doi.org/10.1029/2019JB017918

Mitrovica, J. X. (1996). Haskell (1935) revisited. J. Geophys. Res.: Sol. Earth, 101, 555–569, 10.1029/95JB03208.

Mitrovica, J.X., A.M. Forte, A new inference of mantle viscosity based upon joint inversion of convection and glacial isostatic adjustment data, Earth and Planetary Science Letters, Volume 225, Issues 1–2, 2004, Pages 177-189, ISSN 0012-821X, https://doi.org/10.1016/j.epsl.2004.06.005.

Nerem, R. S., and J. Wahr (2011), Recent changes in the Earth's oblateness driven by Greenland and Antarctic ice mass loss, *Geophys. Res. Lett.*, 38, L13501, doi:10.1029/2011GL047879.

Panasyuk, S. V. & Hager, B. H. (2000a). Inversion for mantle viscosity profiles constrained by dynamic topography and the geoid, and their estimated errors. Geophys. J. Int., 143, 821–836.

Paulson, A., Zhong, S., & Wahr, J. (2005). Modelling post-glacial rebound with lateral viscosity variations. Geophysical Journal International, 163(1), 357–371. https://doi.org/10.1111/j.1365-246x.2005.02645.x

Paulson, A., Zhong, S., & Wahr, J. (2007). Inference of mantle viscosity from GRACE and relative sea level data. Geophysical Journal International, 171(2), 497–508. https://doi.org/10.1111/j.1365-246x.2007.03556.x

Peltier, W. R. (1974), The impulse response of a Maxwell Earth, *Rev. Geophys.*, 12(4), 649–669, doi:10.1029/RG012i004p00649.

Peltier, W. R., D. F. Argus, and R. Drummond (2015), Space geodesy constrains ice age terminal deglaciation: The global ICE-6G_C (VM5a) model [Dataset], J. Geophys. Res. Solid Earth, 120, 450–487, doi:10.1002/2014JB011176.

Peltier, W. R., J. T. Andrews, Glacial-Isostatic Adjustment—I. The Forward Problem, *Geophysical Journal International*, Volume 46, Issue 3, September 1976, Pages 605–646, https://doi.org/10.1111/j.1365-246X.1976.tb01251.x

Peltier, W.R., 2004. Global Glacial Isostasy and the Surface of the Ice-Age Earth: The ICE-5G(VM2) model and GRACE, Ann. Rev. Earth Planet. Sci., 32, 111-149.

Ricard, Y., M. Richards, C. Lithgow-Bertelloni, and Y. Le Stunff (1993), A geodynamic model of mantle density heterogeneity, *J. Geophys. Res.*, 98(B12), 21895–21909, doi:10.1029/93JB02216.

Ritsema, J., Deuss, A., van Heijst, H. J., & Woodhouse, J. H. (2011). S40RTS: A degree-40 shear-velocity model for the mantle from new Rayleigh wave dispersion, teleseismic travel time and normal-mode splitting function measurements [Dataset]. Geophysical Journal International, 184(3), 1223–1236. https://doi.org/10.1111/j.1365-246X.2010.04884.x

Rodell, M., Barnoud, A., Robertson, F.R. *et al.* An Abrupt Decline in Global Terrestrial Water Storage and Its Relationship with Sea Level Change. *Surv Geophys* 45, 1875–1902 (2024). https://doi.org/10.1007/s10712-024-09860-w

Rolf, T., Capitanio, F. A., & Tackley, P. J. (2018). Constraints on mantle viscosity structure from continental drift histories in spherical mantle convection models. Tectonophysics, 746, 339-351.

Rounce, D. R., Hock, R., Maussion, F., Hugonnet, R., Kochtitzky, W., Huss, M., et al. (2023). Global glacier change in the 21st century: Every increase in temperature matters. Science, 379(6627), 78–83. https://doi.org/10.1126/science.abo1324

Roy, K., W.R. Peltier, Space-geodetic and water level gauge constraints on continental uplift and tilting over North America: regional convergence of the ICE-6G_C (VM5a/VM6) models, *Geophysical Journal International*, Volume 210, Issue 2, August 2017, Pages 1115–1142, https://doi.org/10.1093/gji/ggx156

Sasgen, I., Martín-Español, A., Horvath, A., Klemann, V., Petrie, E. J., Wouters, B., Horwath, M, Paio, R., Bamber, J.L. Clarke, P.J., Konrad, H., Drinkwater, M.R. (2017): Joint inversion estimate of regional glacial isostatic adjustment in Antarctica considering a lateral varying Earth structure (ESA STSE Project REGINA). Geophysical Journal International, 211(3), 1534-1553, doi: 10.1093/gji/ggx368.

Schumacher, M., King, M., Rougier, J.C., Sha, Z., Khan, S. A., Bamber, J., L., (2018): A new global GPS dataset for testing and improving modelled GIA uplift rates [Dataset]. PANGAEA, https://doi.org/10.1594/PANGAEA.889923

Soran Parang, Glenn A. Milne, Lev Tarasov, Ryan Love, Maryam Yousefi, Matteo Vacchi, Constraining models of glacial isostatic adjustment in eastern North America, Quaternary

Science Reviews, Volume 334, 2024, 108708, ISSN 0277-3791,
https://doi.org/10.1016/j.quascirev.2024.108708.

Steinberger, B., & O'Connell, R. J. (2002). The convective mantle flow signal in rates of true polar wander. In: *Ice Sheets, Sea Level and the Dynamic Earth*, Eds: J. X. Mitrovica and B. L. A. Vermeersen, *Geodynamics Ser. 29*, 233-256, American Geophysical Union.

Steinberger, B., S. C. Werner, T. H. Torsvik (2010).Deep versus shallow origin of gravity anomalies, topography and volcanism on Earth, Venus and Mars, Icarus, Volume 207, Issue 2, Pages 564-577, ISSN 0019-1035, https://doi.org/10.1016/j.icarus.2009.12.025.

Vacchi, M., Engelhart, S. E., Nikitina, D., Ashe, E. L., Peltier, W. R., Roy, K., et al. (2018). Postglacial relative sea-level histories along the eastern Canadian coastline [dataset]. Quaternary Science Reviews, 201, 124–146. https://doi.org/10.1016/j.quascirev.2018.09.043

van Hunen, J., S. Zhong, N. M. Shapiro, M. H. Ritzwoller, New evidence for dislocation creep from 3-D geodynamic modeling of the Pacific upper mantle structure, Earth and Planetary Science Letters, Volume 238, Issues 1–2, 2005, Pages 146-155, ISSN 0012-821X, https://doi.org/10.1016/j.epsl.2005.07.006.

van Summeren, J., C. P. Conrad, and C. Lithgow-Bertelloni (2012), The importance of slab pull and a global asthenosphere to plate motions, *Geochem. Geophys. Geosyst.*, 13, Q0AK03, doi:10.1029/2011GC003873.

Vondrak J., Ron C., Stefka V. (2010): Earth orientation parameters based on EOC-4 astrometric catalog [dataset], Acta Geodyn. Geomat., https://hpiers.obspm.fr/iers/eop/eopc01/

Wahr, J., R. S. Nerem, and S. V. Bettadpur (2015), The pole tide and its effect on GRACE time-variable gravity measurements: Implications for estimates of surface mass variations, J. Geophys. Res. Solid Earth, 120, 4597–4615, doi:10.1002/2015JB011986.

Weertman J. Rate of Growth or Shrinkage of Nonequilibrium Ice Sheets. *Journal of Glaciology*. 1964;5(38):145-158. doi:10.3189/S0022143000028744

Yuan, T., & Zhong, S. (2024). Dataset for CitcomSVE 3.0: A Three-dimensional Finite Element Software Package for Modeling Load-induced Deformation for an Earth with Viscoelastic and Compressible Mantle. [Dataset]. Zenodo. https://doi.org/10.5281/zenodo.14277856

Yuan, T., Zhong, S. & A, G. CitcomSVE-3.0: a three-dimensional finite-element software package for modeling load-induced deformation and glacial isostatic adjustment for an Earth with a viscoelastic and compressible mantle. Geosci. Model Dev. 18, 1445–1461 (2025).

Yuan, T., Zhong, S. Effects of glacial forcing on lithospheric motion and ridge spreading. *Nature* 641, 122–128 (2025). https://doi.org/10.1038/s41586-025-08846-x

Yuen, D. A., Sabadini, R. C., Gasperini, P., & Boschi, E. On transient rheology and glacial isostasy. Journal of Geophysical Research: Solid Earth, 91(B11), 11420-11438 (1986).

Zhong, S. (2001), Role of ocean-continent contrast and continental keels on plate motion, net rotation of lithosphere, and the geoid, *J. Geophys. Res.*, 106(B1), 703–712, doi:10.1029/2000JB900364.

Zhong, S., Kang, K., A, G., & Qin, C. (2022). CitcomSVE: A three-dimensional finite element software package for modeling planetary mantle's viscoelastic deformation in response to surface and tidal loads. Geochemistry, Geophysics, Geosystems, 23(10), e2022GC010359.

Figure 1.

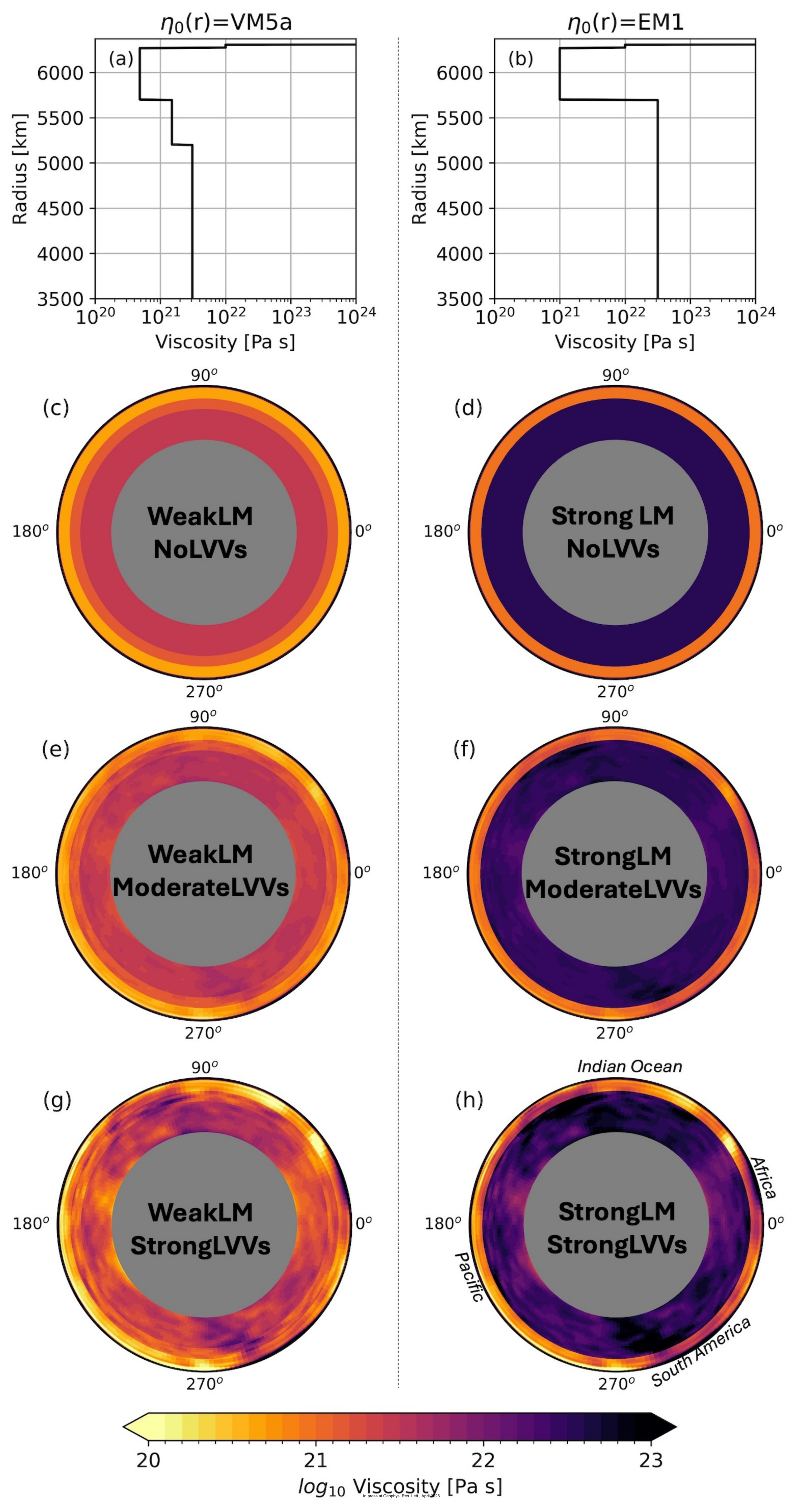
η_0(r)=VM5a
η_0(r)=EM1
(a)
(b)
Radius [km]
6000
5500
5000
4500
4000
3500
10^{20}
10^{21}
10^{22}
10^{23}
10^{24}
Viscosity [Pa s]
(c)
(d)
(e)
(f)
(g)
(h)
90^o
180^o
0^o
270^o
WeakLM NoLVVs
Strong LM NoLVVs
WeakLM ModerateLVVs
StrongLM ModerateLVVs
WeakLM StrongLVVs
StrongLM StrongLVVs
Indian Ocean
Africa
Pacific
South America
20
21
22
23
log_{10} Viscosity [Pa s]

Figure 2.

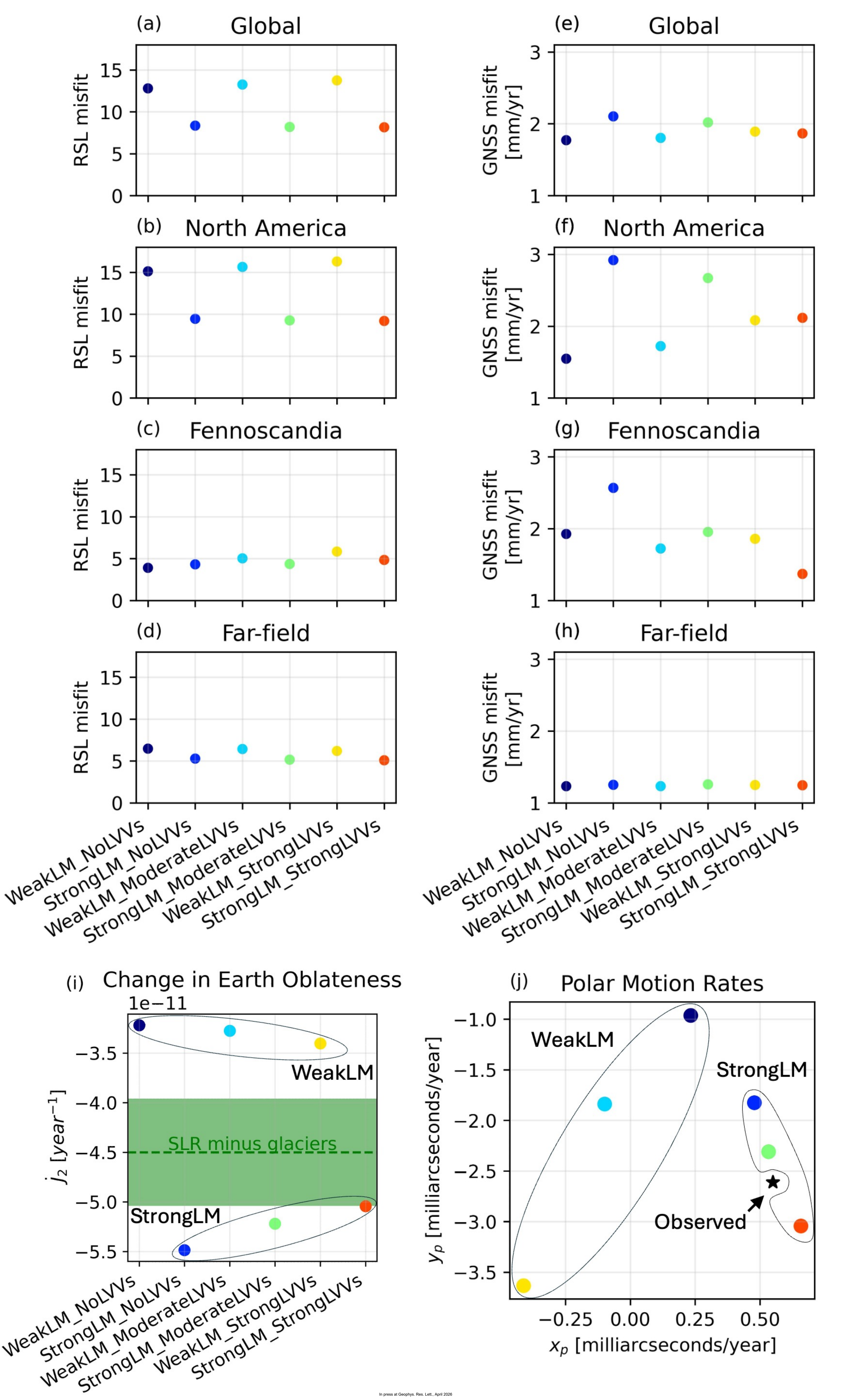
(a) Global
RSL misfit
(b) North America
(c) Fennoscandia
(d) Far-field
(e) Global
GNSS misfit [mm/yr]
(f) North America
(g) Fennoscandia
(h) Far-field
WeakLM_NoLVVs
StrongLM_NoLVVs
WeakLM_ModerateLVVs
StrongLM_ModerateLVVs
WeakLM_StrongLVVs
StrongLM_StrongLVVs
(i) Change in Earth Oblateness
1e−11
$\dot{J}_2$ [year^{-1}]
WeakLM
StrongLM
SLR minus glaciers
(j) Polar Motion Rates
y_p [milliarcseconds/year]
x_p [milliarcseconds/year]
Observed

Figure 3.

GNSS Observations

GIA Model Predictions

Misfits

$VLM_{GNSS}^{(Schumacher)}$

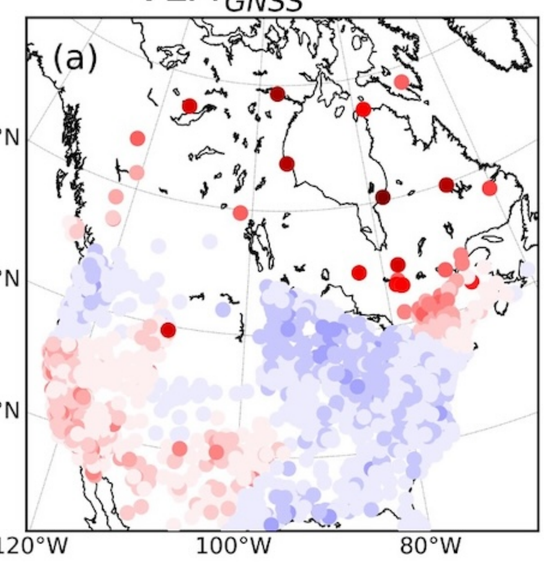

$VLM_{GNSS}^{(Argus)}$

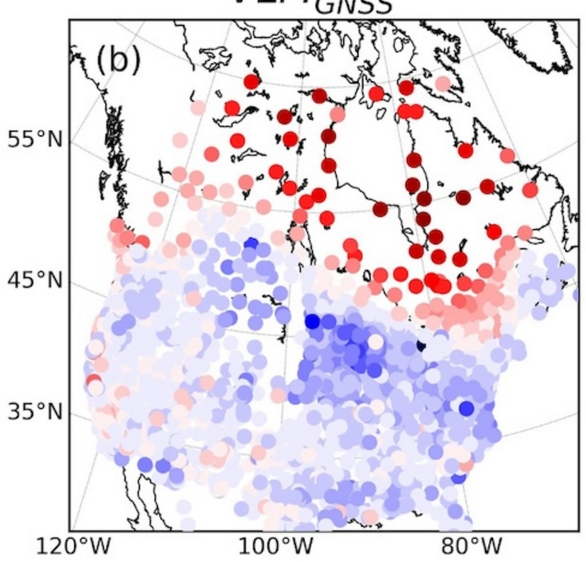

$VLM_{GNSS}^{(Hammond)}$

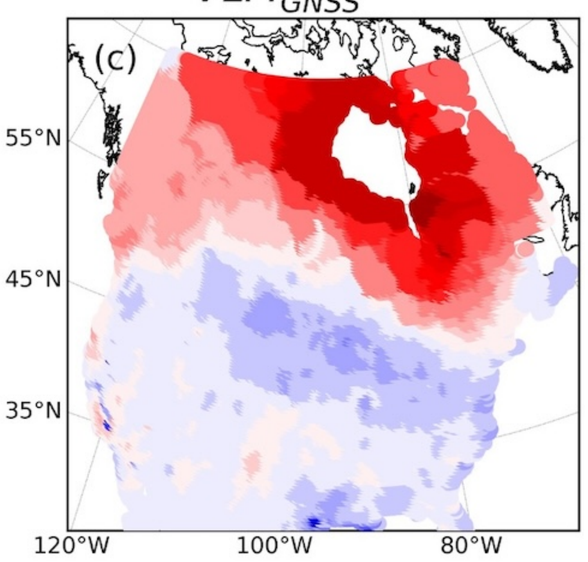

$VLM_{GIA}^{(WeakLM,\,NoLVVs)}$

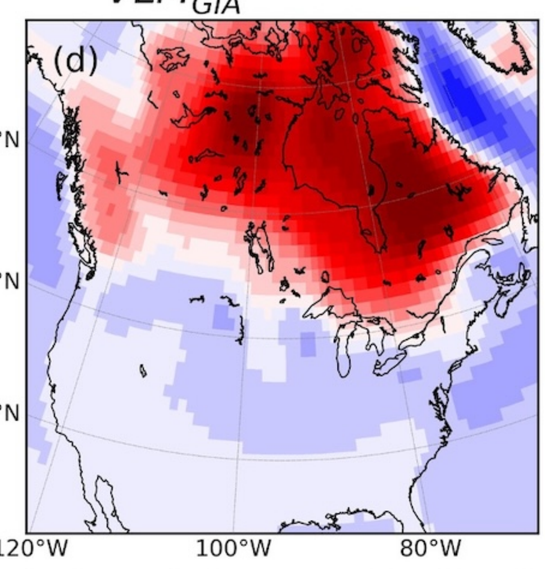

$VLM_{GIA}^{(WeakLM,\,StrongLVVs)}$

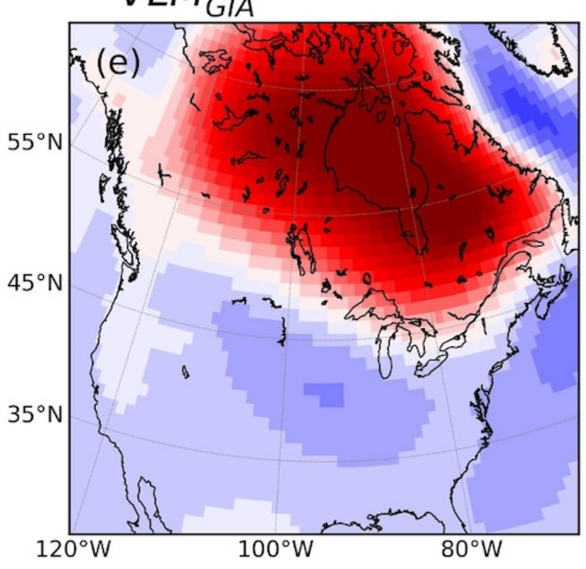

$VLM_{GIA}^{(StrongLM,\,StrongLVVs)}$

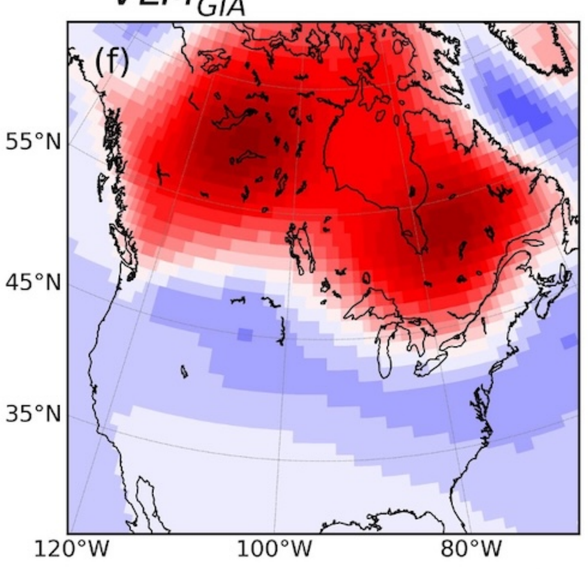

$VLM_{GNSS}^{(Schumacher)} - VLM_{GIA}^{(WeakLM,\,NoLVVs)}$

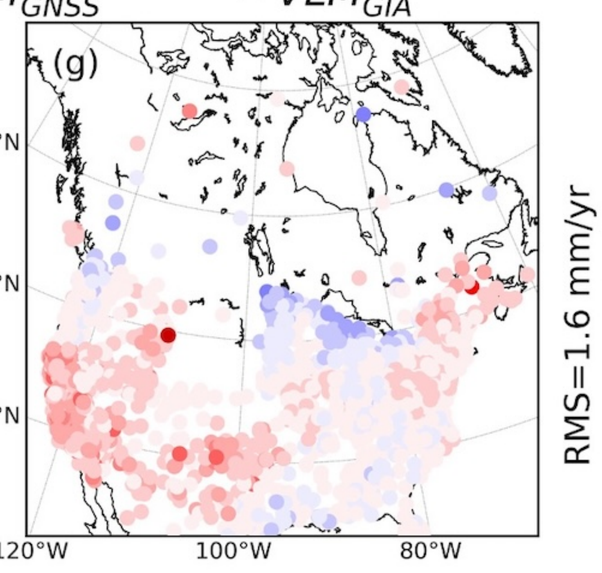

$VLM_{GNSS}^{(Schumacher)} - VLM_{GIA}^{(WeakLM,\,StrongLVVs)}$

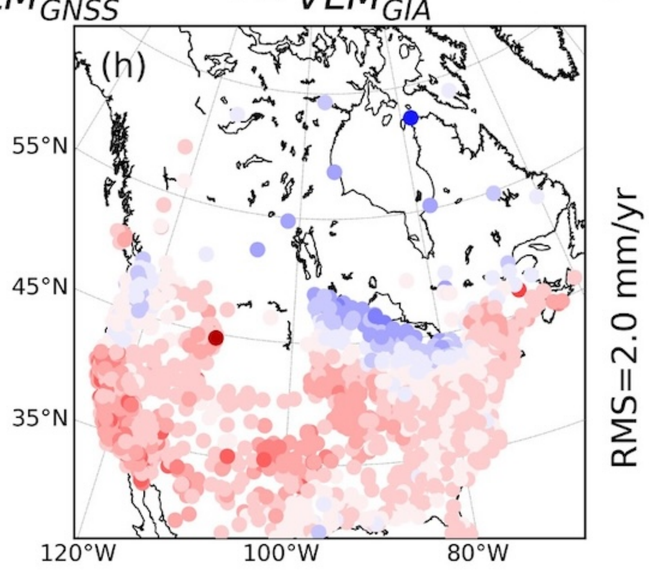

$VLM_{GNSS}^{(Schumacher)} - VLM_{GIA}^{(StrongLM,\,StrongLVVs)}$

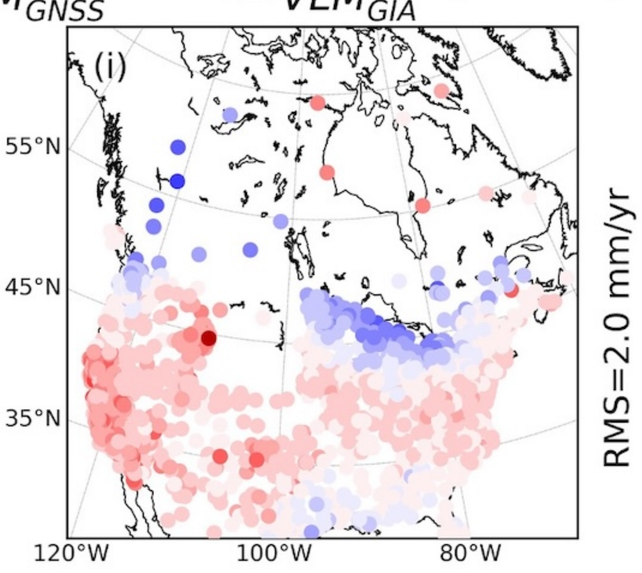

$VLM_{GNSS}^{(Argus)} - VLM_{GIA}^{(WeakLM,\,NoLVVs)}$

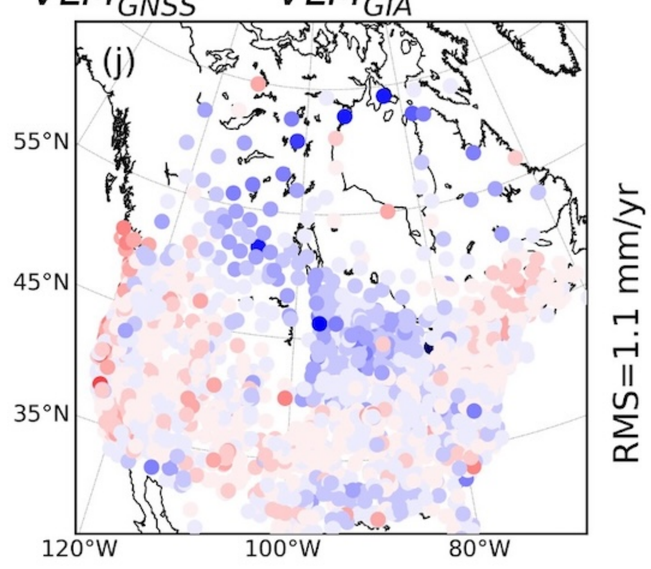

$VLM_{GNSS}^{(Argus)} - VLM_{GIA}^{(WeakLM,\,StrongLVVs)}$

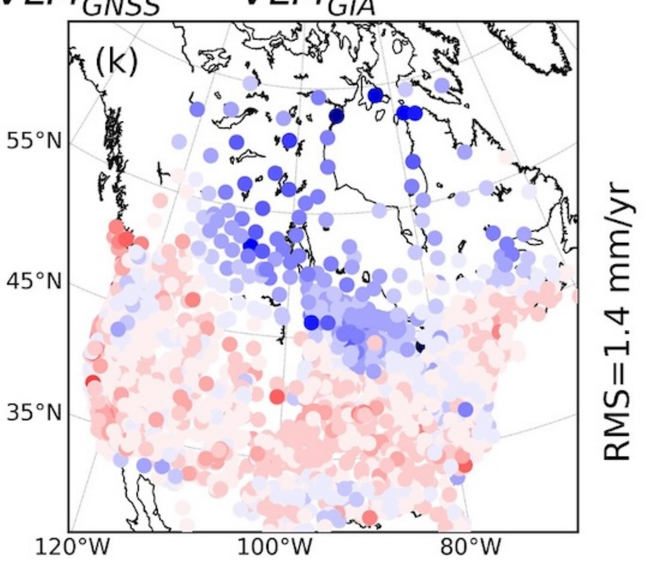

$VLM_{GNSS}^{(Argus)} - VLM_{GIA}^{(StrongLM,\,StrongLVVs)}$

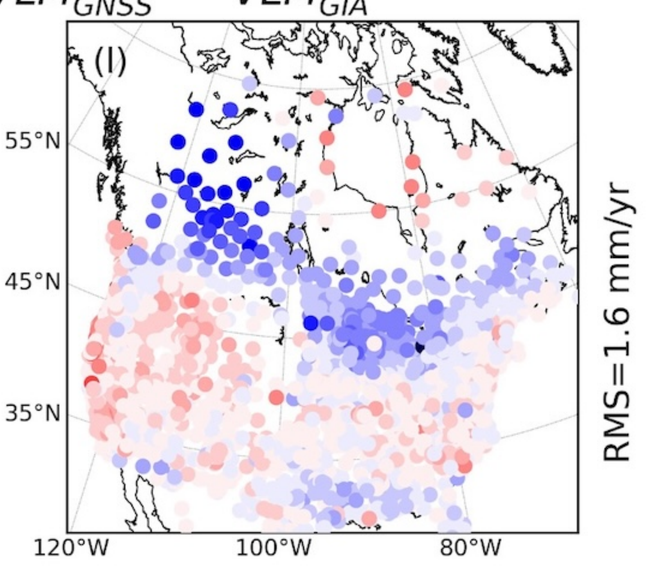

$VLM_{GNSS}^{(Hammond)} - VLM_{GIA}^{(WeakLM,\,NoLVVs)}$

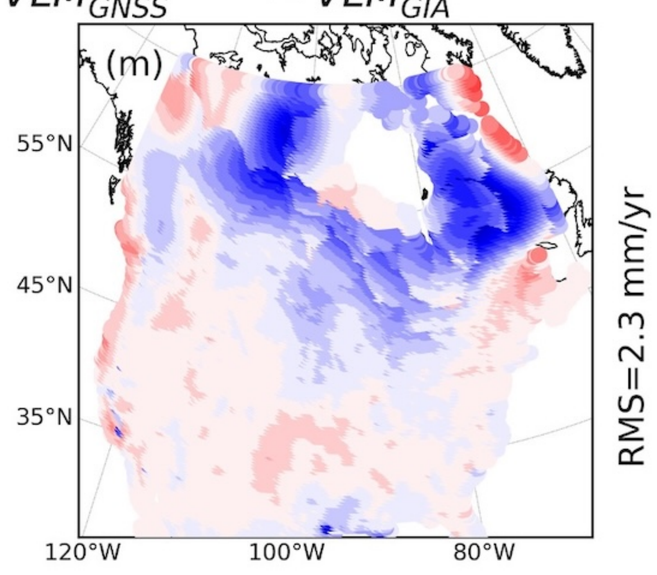

$VLM_{GNSS}^{(Hammond)} - VLM_{GIA}^{(WeakLM,\,StrongLVVs)}$

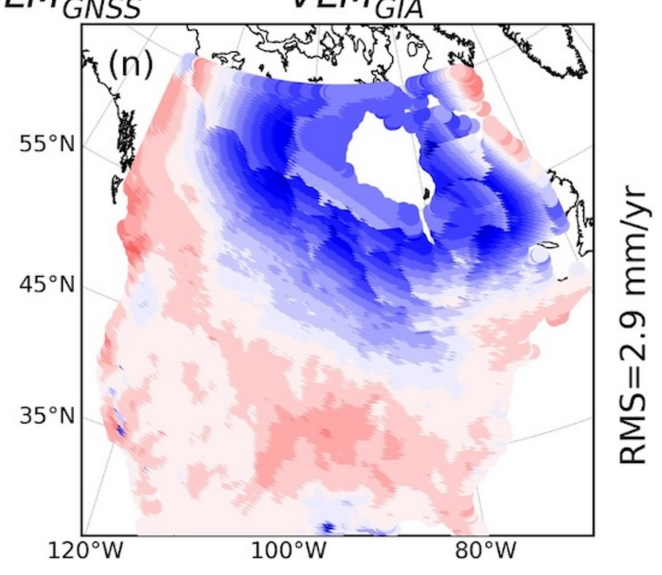

$VLM_{GNSS}^{(Hammond)} - VLM_{GIA}^{(StrongLM,\,StrongLVVs)}$

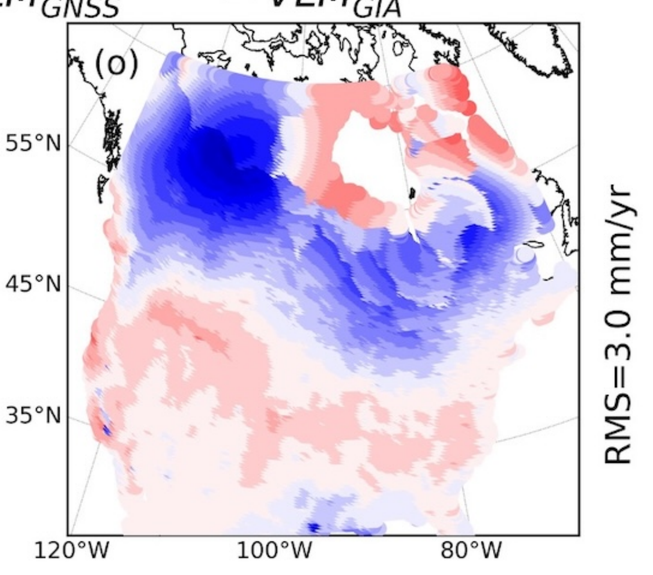

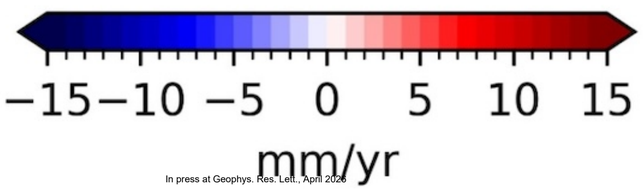

Figure 4.

(a) Regionally Averaged Viscosity

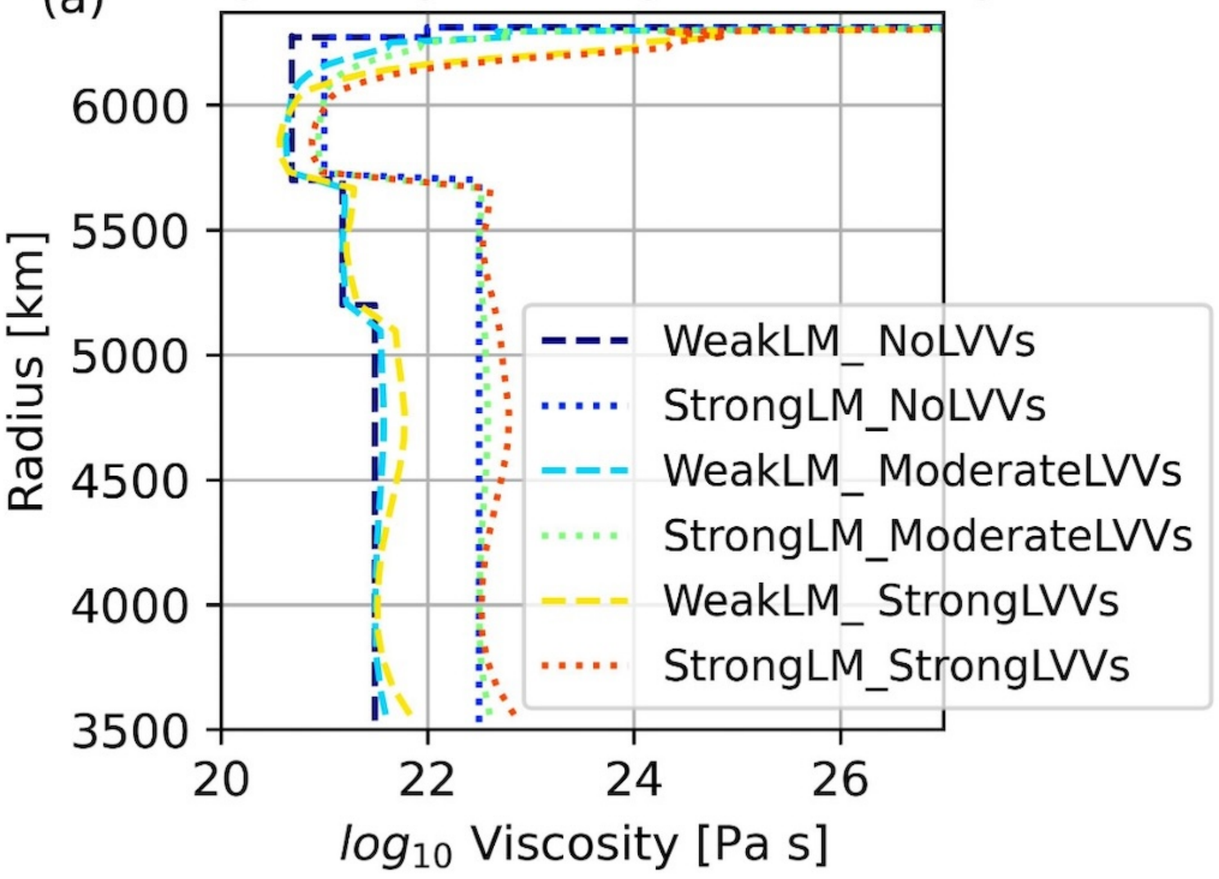

(b) Averaged Region & Transects